 ©2024 Uspekhi Fizicheskikh Nauk, Russian Academy of Sciences

REVIEWS OF TOPICAL PROBLEMS

PACS numbers: **42.82. – m,** 42.82.Et, 84.40.Lj

55th ANNIVERSARY OF THE INSTITUTE OF SPECTROSCOPY OF THE RUSSIAN ACADEMY OF SCIENCES (ISAN)

Silicon integrated photonics

S S Kosolobov, I A Pshenichnyuk, K R Taziev, A K Zemtsova, D S Zemtsov, A S Smirnov, D M Zhigunov, V P Drachev

DOI: https://doi.org/10.3367/UFNe.2024.09.039762

Contents

1. **Introduction** 1153
2. **Methods for calculating integrated components** 1155
3. **Waveguides and microring resonators** 1157
4. **Vernier filters with thermo-optical tuning** 1160
5. **Arrayed waveguide gratings** 1161
6. **Interferometers and electro-optical modulators** 1162
7. **Optical coupling technologies** 1164
8. **Conclusions** 1166

References 1166

Abstract. Technologies of silicon integrated photonics are the basis for the fabrication of a class of devices, such as optical modulators, photodetectors, optical filters and switches, multiplexers and demultiplexers, and optical transceivers. In many respects, silicon integrated photonics competes with alternative platforms based on indium phosphide, silicon nitride and dioxide, and other platforms. Here we provide an overview of modern approaches used in silicon integrated photonic technologies, describe the components of photonic integrated circuits and devices developed on their basis, and make a comparison with alternative technology platforms.

Keywords: silicon, integrated photonics, nanophotonics, silicon-on-insulator, photonic integrated circuits

1. Introduction

Integrated silicon photonics demonstrates a high competitive level among technological platforms focused on the fabrication of photonic integrated circuits (PICs) and devices based on them. Over the past decades, interest in research in the field of silicon photonics has been steadily growing due to wide range of applications such as telecommunications and high-speed data transmission, microwave photonics, as well as sensors, including photodetectors, lidars, gyroscopes, biosensors, and spectrometers. The state of the art of silicon technology provides enormous opportunities for the fabrication of photonic integrated circuits, since it is based on proven technological processes of silicon microelectronics.

An obvious advantage of silicon photonics is its full compatibility with well-developed technologies for the fabrication of microelectronic components, in particular complementary metal–oxide–semiconductor (CMOS) technology [1]. One of the factors intensifying the silicon photonics technology development is the high integration density realization, i.e. ability to increase the quantity elements per chip. Rapid advance of silicon photonics has provided a dramatic increase in the integration of photonic elements [2]. Photonic integrated circuits with a high density of photonic components are developed for applications in the field of telecommunications [3], optical detection [4–6], and on-chip quantum computing [7], as well as for optical phased arrays [8] and other devices. The total number of photonic components on such chips has reached several ten thousand [9]. In terms of the degree of integration, a silicon platform surpasses its closest competitors, for example, platforms based on A_3B_5 or Si_3N_4 technologies.

In addition to a high integration density, photonic technologies Should provide the development of integrated elements with low optical loss, a small size, a high efficiency of optical coupling, low power consumption, a possibility of precise control of phase delays, and a high rate of information exchange with microelectronics elements. This imposes strict requirements on the choice of technological approaches used to design elements of photonic integrated circuits. Currently, integrated photonic components are manufactured on the base of several technological platforms, being developed in parallel. Lithium niobate, A_3B_5 semiconductor structures, silicon oxide and nitride, polymer coatings, and monocrystalline silicon were used as the starting wafers.

S S Kosolobov [(a)], **I A Pshenichnyuk** [(b)], **K R Taziev** [(c)], **A K Zemtsova** [(d)], **D S Zemtsov** [(e)], **A S Smirnov** [(f)], **D M Zhigunov** [(g)], **V P Drachev** [(h)]
Skolkovo Institute of Science and Technology,
Territory of the Skolkovo Innovation Center,
Bol'shoi bul'var 30, str. 1, 121205 Moscow, Russian Federation
E-mail: [(a)] s.kosolobov@skoltech.ru, [(b)] I.Pshenichnyuk@skoltech.ru, [(c)] Kamil.Taziev@skoltech.ru, [(d)] A.Zemtsova@skoltech.ru, [(e)] D.Zemtsov@skoltech.ru, [(f)] Al.Smirnov@skoltech.ru, [(g)] D.Zhigunov@skoltech.ru, [(h)] V.Drachev@skoltech.ru

Received 15 April 2024, revised 12 September 2024
Uspekhi Fizicheskikh Nauk **194** (11) 1223 – 1239 (2024)
Translated by I A Ulitkin

Basic components of silicon photonics are implemented on a silicon on insulator (SOI) which has a number of advantages over other platforms, such as silicon nitride and dioxide, and indium phosphide. The SOI substrate contains a dielectric layer (silicon dioxide) sandwiched between two layers of monocrystalline silicon — a topmost device layer and handle wafer. The handle wafer is usually made of the same material as the device layer. Due to the transparency of silicon in the IR spectral range and a large ($n_{\rm Si} \sim 3.4$) refractive index compared to that of silicon dioxide ($n_{\rm SiO_2} \sim 1.5$), the silicon-on-insulator structure ensures localization of the optical mode in the device layer of silicon. A high optical contrast of silicon–dielectric materials also determines the compactness of the manufactured integrated optical elements and, consequently, their high density on a chip. In addition to compactness, the difference in refractive indices allows the light to be efficiently manipulated in the vertical direction and opens the route for the developing the elements based on optical interference, metasurfaces, and diffraction grating. For silicon photonic devices, the most widespread SOI wafers contain device layers of 220 or 500 nm thickness. These typical sizes are determined by the transverse size of the optical mode propagating in silicon. SOI wafers with a different thickness of the device layer can be used for the fabrication of multimode integrated optical waveguides.

Important advantages include a possibility of manufacturing large (up to 300 mm) diameter SOI wafers, which significantly exceed the wafer sizes achievable on alternative platforms [1, 10]. In addition to the above properties, the high quality of silicon — characterized by low impurity concentrations — and well-developed technologies for structuring this material make it possible to fabricate elements with minimal roughness of waveguide sidewalls, which ensures low optical propagation losses in combination with a small size of integrated optical components.

A possibility of heterogeneous integration of silicon photonic integrated circuits with other platforms using direct bonding technology allows the range of possible applications of such devices to be significantly expanded. This approach does not have limitations that arise with monolithic integration, when it is necessary to take into account the mismatch of crystal lattice parameters and differences in the symmetry of unit cells of different materials.

Integrated silicon photonics technologies are based on structuring substrates using lithography techniques. As noted above, the high quality of original silicon substrates with a low concentration of impurities and structural defects ensures propagation losses in optical components fabricated on these substrates. The most significant contribution to optical losses is due to the quality of manufacturing of integrated elements rather than by the bulk material itself. In particular, the roughness of waveguide sidewall has of great importance [11, 12]. The effect of roughness becomes more significant with a decrease in the lateral size of the waveguide due to enhanced interaction of the optical mode propagating in a waveguide with a sidewall.

With the help of photo- or electron-beam lithography in combination with plasma etching processes the integrated optical elements such as single-mode and multimode waveguides, diffraction gratings, microring resonators, splitters and combiners, Mach–Zehnder and Fabry–Pérot interferometers, spectrally selective elements (arrayed waveguide gratings, Bragg filters) and other components are fabricated on the surface of silicon substrates [13]. Silicon-on-insulator substrates are also widely used in modern microelectronics technology, which makes it possible to integrate photonics devices with semiconductor microelectronics components [14].

After the formation a mask in the resist layer by means of e-beam lithography technique, the substrate is structured using inductively coupled plasma (ICP) etching. To this end, use is made of plasma etching facilities with an inductively coupled plasma (ICP) source. The ICP source in such a facility allows one to produce plasma with a high, more than 10^{15} cm^{-3}, volume density. A distinctive feature of plasma etching systems with inductively coupled plasma is the ability to independently control the density of active particles in the plasma and their kinetic energy when interacting with the sample surface. Independent control is implemented by applying voltage to an additional electrode located on the sample holder, accelerating active radicals towards the sample surface. Unlike systems with reactive ion etching, this enables high rates of plasma etching of silicon due to the generation of high-density plasma, precise control of the selectivity of the process, and precise control of the isotropy of the etching process affecting the verticality of the fabricated element profile.

Alternative platforms, such as those based on A_3B_5 semiconductors, provide exciting opportunities for monolithic integration of optical integrated elements with light-emitting and photodetecting components. The direct-band structure of A_3B_5 materials ensures the fabrication of highly efficient semiconductor lasers and photodetectors, while adaptation of hetero-epitaxial growth conditions makes it possible to regulate the band diagram and, consequently, the optical properties of the manufactured heterostructures. Epitaxially grown A_3B_5 materials have optical loss comparable to silicon, which makes this platform attractive for the manufacture of passive integrated optical elements and interference coatings. Unlike silicon, ternary and quaternary solutions of A_3B_5 semiconductors allow the refractive index to be controlled over a wide range and to be modulated in space. Note, however, that the content of group IV elements in Earth's crust is significantly higher than that of other materials. Thus, silicon makes up 27% of the mass of Earth's crust, while, for example, the abundance of indium is only 0.000005%. In general, it can be stated that A_3B_5 materials are undoubtedly in the lead in optoelectronic devices requiring high optical powers, while integrated optical elements based on silicon platforms are preferable in the field of optical signal processing, including division, summation, operations with radiation polarization, multiplexing, demultiplexing, and other operations for compact optoelectronic integrated devices with very high production volumes.

This review is devoted to the analysis of the current state in the field of silicon integrated photonics. Particular interest in this area is due to the close connection between fundamental research and practical application in the development of photonic integrated circuits and systems based on them. In particular, this concerns the properties of optical radiation localized in submicron and nanometer layers of silicon and hybrid structures. The review includes the following topics. Section 2 describes methods for theoretical numerical calculation of integrated components of photonic integrated circuits. Section 3 examines work devoted to the development of integrated waveguides with minimal optical loss and microring resonators. Section 4 discusses achievements in the field of designing integrated tunable optical filters. Section 5

provides general information about arrayed waveguide gratings that perform multiplexing and demultiplexing of optical signals, which is of great practical importance for telecommunication applications. Section 6 analyzes existing integrated interferometers and optical modulators provide active control of the phase and intensity of light propagating in photonic integrated circuits. Finally, Section 7 discusses problems with optical radiation input–output in photonic integrated circuits.

2. Methods for calculating integrated components

Before fabrication photonic integrated circuit components, optical characteristics of elements are calculated numerically using commercially available and specially developed proprietary software. In integrated photonics, we usually deal with electromagnetic radiation localized in space volumes with the characteristic sizes which are close to the diffraction limit. In this case, the role of near fields is significant and even decisive, and the wave properties of light come to the fore. In such regimes, the basic theory describing the propagation of light, as well as its interaction with matter, is expressed by Maxwell's macroscopic equations [15, 16]. To construct realistic three-dimensional models, the equations are usually solved numerically. There are many different approaches and computational algorithms, each with its own advantages and disadvantages [17]. In addition, there is a wide choice of the available solvers. In this paper, we used the Comsol Multiphysics v.5.3a package with the additional Wave Optics module to calculate integrated components. Below, we consider two popular computational approaches used in simulations of photonic devices.

One of the methods directly used in numerical simulation is based on a system of two Maxwell's equations:

$$\nabla \times \mathbf{E} = -\mu_0 \mu_r \frac{\partial \mathbf{H}}{\partial t}\,, \tag{1}$$

$$\nabla \times \mathbf{H} = +\varepsilon_0 \varepsilon_r \frac{\partial \mathbf{E}}{\partial t} + \sigma \mathbf{E}\,. \tag{2}$$

Here, $\mathbf{E}$ and $\mathbf{H}$ denote electric and magnetic field, respectively. Moreover, in addition to the fundamental constants ε_0 and μ_0, the equations include such important characteristics of continuous media as the relative permittivity ε_r and magnetic permeability μ_r, as well as the specific conductivity σ. Note that the appearance of relative permittivity and magnetic permeability in the given form in equations (1) and (2) implies a linear response of the medium to an electromagnetic perturbation. In addition, when deriving these equations, the time dependence of permittivity and magnetic permeability is ignored, thereby eliminating time dispersion. In this case, the values of ε_r and μ_r are selected in accordance with the frequency of the radiation source. Since, in the general case, approach (1)–(2) allows the frequency to vary during the simulation process, this can lead to a number of computational difficulties and limitations [17]. Such difficulties do not arise when simulation is performed in the frequency space (see below), where the frequency ω is a parameter of the equation which allows one to unambiguously fix the values of permittivity and magnetic permeability.

To describe more complex effects, for example, to take into account nonlinear properties of materials or anisotropy, the equations require generalization [18]. At the same time, the linear equations presented above allow one to describe a wide class of effects and model the main components of photonic circuits. System (1)–(2) contains six scalar equations and six unknown components of the electric and magnetic field vectors, i.e., it is self-sufficient and allows a direct numerical solution. When use is made of a Yee lattice to discretize these equations in the finite-difference scheme [17], we obtain an algorithm known in the literature as the finite difference time domain (FDTD) method, which is actively engaged in the practice of simulating elements of photonic integrated circuits.

Here, we present one of the discretization methods using a finite-difference approach as applied to equations (1) and (2). To make the formulas more compact, we consider a two-dimensional space and disregard the derivatives with respect to z. As is known, six scalar equations are divided in this case into two independent groups corresponding to different polarizations of light. We will consider a group that includes two components of the electric field (E_x and E_y) and one component of the magnetic field (H_z), which corresponds to the TM polarization. In addition, we will assume that there are no conducting materials in the system, which allows us to set $\sigma = 0$. We obtain three scalar equations:

$$\frac{\partial H_z}{\partial t} = \frac{1}{\mu}\left(\frac{\partial E_x}{\partial y} - \frac{\partial E_y}{\partial x}\right), \tag{3}$$

$$\frac{\partial E_x}{\partial t} = \frac{1}{\varepsilon}\frac{\partial H_z}{\partial y}\,, \tag{4}$$

$$\frac{\partial E_y}{\partial t} = -\frac{1}{\varepsilon}\frac{\partial H_z}{\partial x}\,. \tag{5}$$

Here, we use the notations $\varepsilon \equiv \varepsilon_0 \varepsilon_r$ and $\mu \equiv \mu_0 \mu_r$. Moving from continuous coordinates (x, y, t) to discrete ones (i, j, n) and rewriting the derivatives in the form of finite differences, we obtain the equations

$$\frac{H_z\big|^{n+1/2}_{i+1/2,\,j+1/2} - H_z\big|^{n-1/2}_{i+1/2,\,j+1/2}}{\Delta t} = \frac{1}{\mu_{i+1/2,\,j+1/2}} \times \left[\frac{E_x\big|^{n}_{i+1/2,\,j+1} - E_x\big|^{n}_{i+1/2,\,j}}{\Delta y} - \frac{E_y\big|^{n}_{i+1,\,j+1/2} - E_y\big|^{n}_{i,\,j+1/2}}{\Delta x}\right], \tag{6}$$

$$\frac{E_x\big|^{n+1}_{i+1/2,\,j} - E_x\big|^{n}_{i+1/2,\,j}}{\Delta t} = \frac{1}{\varepsilon_{i+1/2,\,j}}\left[\frac{H_z\big|^{n+1/2}_{i+1/2,\,j+1/2} - H_z\big|^{n+1/2}_{i+1/2,\,j-1/2}}{\Delta y}\right], \tag{7}$$

$$\frac{E_y\big|^{n+1}_{i,\,j+1/2} - E_y\big|^{n}_{i,\,j+1/2}}{\Delta t} = -\frac{1}{\varepsilon_{i,\,j+1/2}}\left[\frac{H_z\big|^{n+1/2}_{i+1/2,\,j+1/2} - H_z\big|^{n+1/2}_{i-1/2,\,j+1/2}}{\Delta x}\right]. \tag{8}$$

These formulas form a ready-made method for implementing a computational algorithm. Having a distribution of fields in space at the initial moment of time ($H_z|^{n-1/2}, E_x|^n, E_y|^n$) and using formulas (6)–(8), we can obtain the distribution of fields at the next moment of time ($H_z|^{n+1/2}, E_x|^{n+1}, E_y|^{n+1}$). Iterative repetition of the procedure reproduces the evolution of the system in the required time window. We emphasize that, when the Yee lattice is used for discretization, a shift is introduced between the grids for the components of the electric and

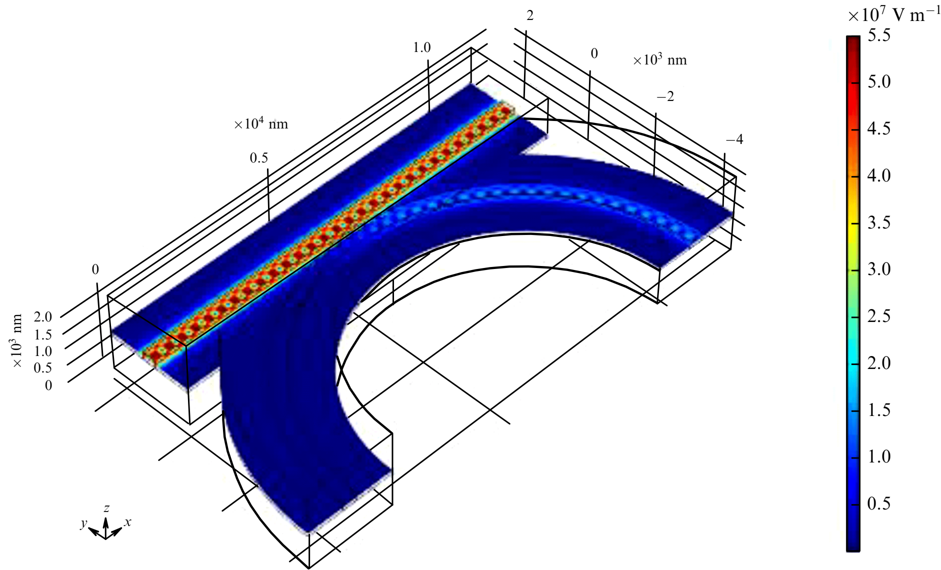

Figure 1. Electrical field modulus [V m^{-1}] of a directional coupler calculated numerically in frequency space. Cross section of silicon waveguide is 220 by 400 nm. Radius of curvature of coupled waveguide is 5300 nm. Gap between two waveguides is 152 nm. Radiation wavelength is 1550 nm.

magnetic fields. The magnitude of the shift is half the selected step in coordinate and time (Δx, Δy, and Δt). This fact is reflected in the appearance of the term $1/2$ in the discrete superscripts. Note also that, for the implementation of the general computational method (as opposed to the special case considered here), there are many different discretization methods, as well numerous computational subtleties and techniques. Since it is impossible to consider them in this paper, we refer the reader to the relevant literature [17].

The problem of electromagnetic field distribution in nanostructures can also be transferred from time space to frequency space. To this end, we introduce an additional assumption that the fields are harmonic in time, i.e., $\mathbf{E}(\mathbf{r}, t) \to \mathbf{E}(\mathbf{r}) \exp(-\mathrm{i}\omega t)$, $\mathbf{H}(\mathbf{r}, t) \to \mathbf{H}(\mathbf{r}) \exp(-\mathrm{i}\omega t)$. Applying the specified substitution in equations (1) and (2), we obtain

$$\nabla \times \mathbf{E} = +\mathrm{i}\omega\mu_0\mu_\mathrm{r}\mathbf{H}\,, \tag{9}$$

$$\nabla \times \mathbf{H} = -\mathrm{i}\omega\,\varepsilon_0\varepsilon_\mathrm{r}\mathbf{E}\,. \tag{10}$$

In these equations, the permittivity is redefined as follows: $\varepsilon_\mathrm{r} + \mathrm{i}\sigma/\omega\varepsilon_0 \to \varepsilon_\mathrm{r}$. Due to this substitution, conductivity σ is excluded from the equation, and permittivity becomes complex. It is worth noting that, after the switching to frequency space, the intensities themselves also become complex, and this should be taken into account when returning to time space. Next, by applying the vector differential operator curl to both parts of (9) and substituting (10) into (9), we obtain the well-known wave equation in frequency space:

$$\nabla \times \frac{1}{\mu_\mathrm{r}}\,\nabla \times \mathbf{E} = \varepsilon_0\mu_0\varepsilon_\mathrm{r}\omega^2\,\mathbf{E}\,. \tag{11}$$

This equation can also be solved using the finite-difference scheme or the finite volume method. It does not contain time derivatives, which significantly simplifies the solution. In addition, instead of six first-order scalar equations in the FDTD scheme, we obtain three second-order scalar equations. In a homogeneous space, where the permittivity and magnetic permeability do not depend on the coordinate, this equation can be simplified and transformed into the Helmholtz equation often used in analytical calculations. However, for three-dimensional numerical simulation, where we explicitly take into account the parameters of various materials and their boundaries, equation (11) is better suited.

These calculation methods are actively used both in frequency space and in time space to simulate photonic devices. The advantages of one method or another depend on many factors. From the point of view of numerical calculation, the two specified approaches have different requirements for the amount of necessary operational memory and have different convergence rates, which are determined by a specific model. From the physical point of view, simulation in time space provides more control over radiation sources, allowing them to be switched on and off at specified times, as well as to change their frequency while observing the propagation of the wave front and the system response at the output as a function of time. In frequency space, it is necessary to fix the frequency as a parameter of the equation, and be content with the final stable state established in a real system after a certain — sometimes quite large — period of time. In the absence of the need to observe the dynamics of the system, when the main goal is to obtain exclusively stationary parameters of the device (transmittance, S matrix, etc.), this approach turns out to be quite applicable. Additional details and examples of the application of computational schemes to specific problems can be found elsewhere [19–21].

As a demonstration of three-dimensional simulation, we present the result for a directional coupler in frequency space (Fig. 1). The figure shows the distribution of the electric field modulus. The color scale can be used to estimate the fraction of radiation transferred from the straight waveguide to the bent one (in this example, it is 12% of power). Similarly, basic elements of photonic circuits, such as waveguides, ring resonators, and waveguide gratings, are simulated.

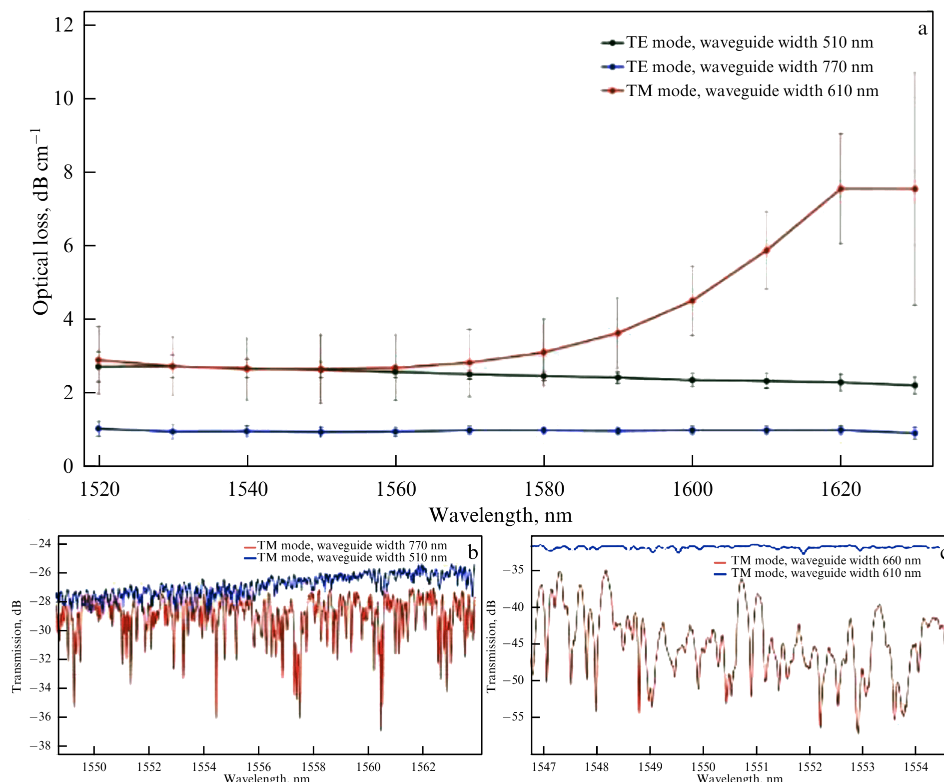

Figure 2. (a) Spectral dependence of optical losses for three types of waveguide geometry, (b) optical transmission of waveguides 37 mm in length and 510 and 770 nm width for TE mode, and (c) optical transmission spectrum of waveguides 37 mm in length and 610 and 660 nm width for TM mode.

3. Waveguides and microring resonators

A basic element of integrated photonics is an optical waveguide that provides transmission of an optical signal from one point of the chip to another. Depending on applications, both single-mode and multimode waveguides are used [22, 23]. For the optical range of 1500–1600 nm, TE-polarized single-mode silicon waveguides fabricated on the SOI platform with a device layer 220 nm in height, have 300–500 nm width. For single-mode silicon waveguides with height of 220 nm, designed to transmit TM-polarized radiation, the waveguide width is typically about 450–500 nm [24]. On the SOI platform with a device layer 500 nm in height, the width of the single-mode waveguide for TM-polarized radiation is 220 nm.

An important characteristic of integrated optical waveguides is the optical losses per unit length of the waveguide. For experimental measurement of this parameter, a series of waveguides of different lengths (in our case, for example, 8, 22, and 37 mm) are fabricated on the surface of an SOI sample with a 220-nm-thick silicon layer using electron beam lithography. Optical coupling is implemented using diffraction gratings. Preference is given to the most technologically advanced geometries with straight grooves fabricated in a single etching step. These gratings provide coupling of TE- or TM-polarized radiation from a lensed optical fiber into an integrated silicon waveguide with an efficiency of more than 50% [25]. The transmission spectra of the fabricated structures in the wavelength range of 1520–1630 nm were measured using a probe station, optical probes, and a BOSA-400 optical analyzer (Aragon Photonics). The obtained spectra are approximated by first six partial sums of the Fourier series to average random oscillations. Dependences of optical transmission on the geometric length of the waveguides allow to estimate spectral optical losses. Figure 2a shows spectral dependences of optical losses for different waveguide lengths. Losses for the TE mode in a 510-nm-wide waveguide were estimated to 2.6 ± 0.2 dB cm^{-1} and for the TM mode in a 610-nm-wide waveguide were 2.6 ± 0.9 dB cm^{-1}, at a wavelength of 1550 nm. The obtained values are close to the smallest optical losses reported in the literature for silicon waveguides of similar geometric dimensions [11, 26]. In papers [12, 14], optical losses of less than 2 dB cm^{-1} was demonstrated in waveguides with a transverse size of less than 500 nm and a height of 220 nm. It was found that, in the short-wavelength part of the spectrum (less than 1560 nm), the values of optical losses for the TE and TM modes are close, but with an increase in wavelength over 1560 nm, the optical losses for the TM mode increase to 7.5 ± 3.1 dB cm^{-1}. At the same time, for the TE mode, there is a noticeable decrease in optical losses to 2.2 ± 0.2 dB cm^{-1}.

With an increase in the width of the silicon waveguide from 510 to 770 nm, the optical losses for the TE mode decreases by almost three times, to 0.9 ± 0.1 dB cm^{-1}. However, for waveguides with a width of 770 nm, oscillations are observed in the transmission spectrum, the amplitude of which can reach 10 dB (Fig. 2b). A similar effect is observed for the TM mode with an increase in the waveguide width from 610 to 660 nm (Fig. 2c). The appearance of such oscillations can stem from a violation of the single-mode conditions with an increase in the waveguide width and the occurrence of intermode interference [22].

Several methods for reducing optical losses in silicon waveguides are used in the manufacture of photonic integrated circuits. One of them is based on reducing the waveguide sidewall roughness by optimizing the fabrication

technology. For example, use is made of methods for optimizing exposure [27], plasma-chemical etching [28, 29], and post-processing in the form of annealing in hydrogen [30, 31], liquid chemical oxidation [32], selective oxidation [33], chemical oxidation at high temperatures [34, 35], and anisotropic etching [36]. With the use of these approaches, the waveguide sidewall roughness is significantly reduced and reaches values on the order of 1–2 nm [37–39], and the values of optical losses in the waveguides are reduced to 0.3 dB cm^{-1} [33] and 0.28 dB cm^{-1} [40].

Shallow-etched optical waveguides (rib-shaped waveguide) are characterized by lower optical losses. For example, Dong et al. [41] demonstrated the optical losses of 0.274 dB cm^{-1} in shallow-etched silicon waveguides with a cross section of 250 nm by 2000 nm. However, a more complex technology must be used to manufacture such waveguides, since the formation of ribs requires careful control of the etching rate of the material and high etching uniformity over the wafer diameter [13]. In addition, shallow-etched waveguides are more sensitive to the bending segments curvature, since localization of the optical mode in such waveguides is weakened. This leads to the need to increase the bending radii, compared to fully etched waveguides, to several ten microns [41].

For comparison, Table 1 shows some typical and minimum values of optical losses in integrated waveguides implemented on various technological platforms.

The optical losses in silicon integrated waveguides at a level of about 2 dB cm^{-1} is an acceptable value for relatively small photonic integrated circuits with a total waveguide length of several millimeters. However, for some elements, such as high-Q integrated microring resonators, such optical losses can restrict the final characteristics. The area of application of microring resonators includes passive and tunable optical filters [50–52], sensors [53–55], and electro-optic modulators [56].

A microring resonator is formed by bending a waveguide into a circle, normally coupled to one or more straight waveguides. The appearance of optical resonances is determined by the condition of the formation of an integer number of radiation wavelengths along the length of the optical path in the ring waveguide. The resulting optical resonance manifests itself in the optical spectrum either at the output of the adjacent waveguide as a dip or at the output of the second straight waveguide as a peak with a Lorentzian shape. For practical applications, the distance between resonances (free spectral range, FSR), the depth of resonances, and their quality factor (Q-factor) are important [24]. As noted above, one of the advantages of the silicon technology platform is the high contrast of the refractive index of silicon compared to that of the environment (usually air or silicon dioxide). This allows the fabrication of small microring resonators with a radius of down to 1.5 μm, which corresponds to an FSR of about 62 nm [57].

Table 1. Optical loss in integrated waveguides manufactured on different platforms.

Technological platform	Waveguide loss, dB cm^{-1}	
	Typical	Minimum
Silicon on insulator (SOI) [42, 43]	0.5 – 2	0.016
Indium phosphide InP [44, 45]	2 – 3	0.4
Silicon nitride Si_3N_4 [46, 47]	0.05 – 0.5	0.0005
Lithium niobate on insulator (LNI) [48]	0.6 – 1	0.027
Silicon dioxide SiO_2 [49]	0.017	—

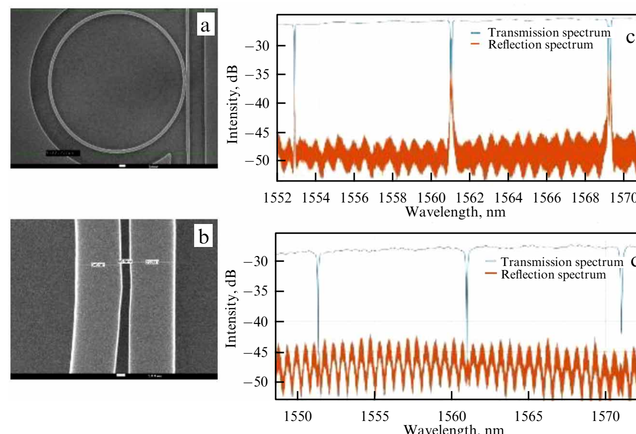

Figure 3. (a, b) SEM images of integrated microring resonator with a radius of 10.7 μm; optical transmission and reflection spectra of microring resonator for (c) TE- and (d) TM-polarized radiation.

Microring resonators fabricated on the SOI platform were studied in various configurations with radii from 3 μm to 5 mm for TE- and TM-polarized optical radiation. Figures 3a and 3b show SEM images of a microring resonator with a radius of 10.7 μm. Optical spectra of the microring resonators for TE and TM polarizations are shown in Figs 3c and 3d, respectively. The microring resonators for the TE and TM polarizations differ in their spectra. Note that resonances are also observed in the reflection spectrum of the microring resonator for the TE mode, and some resonances are splitted (Fig. 3c). This effect is due to backscattering on the sidewall sidewall roughness of the ring waveguide, and it is described qualitatively and quantitatively using known techniques [58, 59]. At the same time, resonances of the TM mode are not splitted and are hardly observed in the reflection spectra (Fig. 3d). This is explained by the fact that the TM mode predominantly interacts with the upper and lower boundaries of the waveguides and barely interacts with the sidewall roughness [60].

Microring resonators optimized for TE- and TM-polarized radiation differ in their geometric parameters. According to calculations, the resonance depth has a maximum depending on the gap size between the microring and straight waveguides. Experimental studies show that, for TE-polarized single-mode resonators with one rectilinear waveguide 500 nm in width, the maximum resonance depth (> 20 dB) is observed for gaps between the microring and the waveguide in the range from 100 to 250 nm, which corresponds to theoretical calculations. The resonance depth depends, among other things, on the length of the ring waveguide and optical losses in it. For TM-polarized light propagating in a microring resonator with a waveguide width of 550 nm, the maximum resonance depth is observed for a gap in the range from 450 to 650 nm. According to calculations, the Q-factor of the resonator increases with increasing gap size and length of the optical path in the ring waveguide and with decreasing total loss in the waveguide [24]. For example, for a single-mode TM resonator 10.7 μm in radius with one straight

waveguide 550 nm in width, an increase in the gap size from 350 to 530 nm led to an increase in the Q-factor from 1.0×10^4 to 3.7×10^4. In experiments with single-mode TM resonators with one straight waveguide, the Q-factor was $\sim 4.2 \times 10^4$ with a resonance depth of 10 dB for waveguides with a width of 550 nm, a gap of 510 nm, and a ring radius of 10.7 μm. Note that, since the resonances are sufficiently deep, the gap between the waveguide and the microring can be increased, and this is important for the technological reproducibility of such elements.

In experiments with single-mode TE resonators having one straight waveguide, the Q-factor was $\sim 10^5$, while the resonance depth was ~ 1.5 dB for 520-nm-wide waveguides with a gap of 210 nm and a ring radius of 10.7 μm. It was found that all resonances for microring resonators with such a Q-factor are splitted. Obtaining unsplit resonances with a Q-factor higher than 10^5 is possible by increasing the length of the microring resonator and using incompletely etched waveguides [61] or multimode waveguides [62, 63]. Note that an increase in the optical path length in a microring resonator will inevitably lead to a decrease in the FSR.

As noted above, the use of methods for reducing optical loss in waveguides, for example by adding post-processing operations, can lead to an increase in the Q-factor of microring resonators. Thus, an improvement in the Q-factor of microring resonators was shown in papers [47, 64], where local oxidation technology was used. Blumenthal et al. [65] demonstrated a microring resonator with a diameter of 9 μm and a Q-factor of 9.2×10^5, which corresponds to a resonance peak width at half maximum of 1.6 pm and an optical loss of 0.76 dB cm^{-1}. It should be noted that such a high Q-factor was obtained using two-stage electron-beam lithography, where the accuracy of matching the patterns of two successive lithographs is better than 25 nm, and plasma-chemical etching in inductively coupled plasma. Subsequent isotropic chemical etching in hydrofluoric acid vapor was used to remove the dielectric layer under the silicon waveguides and form a suspended resonator. However, such changes in technology may not always ensure reproducibility of the final optical characteristics of the designed elements.

An alternative way to improve the Q-factor of microring resonators and, accordingly, reduce optical loss is to decrease the interaction of the optical mode with the waveguide boundaries in order to reduce the scattering of light at the sidewall roughness. For example, for waveguides fabricated on a silicon nitride platform with a height of 175 nm, the optical losses are about 0.1–0.2 dB cm^{-1} [66]. Increasing the aspect ratio (width:height $> 10:1$) leads to a decrease in optical loss to 0.001 dB cm^{-1} [67]. This is due to a decrease in the scattering of the optical mode of light on the sidewalls, since the area of the sidewalls also decreases. On the other hand, the area of the upper and lower faces increases, but, due to the technological features of manufacturing silicon nitride and SOI wafers, the roughness of the planar surfaces is much lower (~ 0.3 nm) [39, 67] than that of the sidewalls ($\sim 1-10$ nm) [11, 37–39]. As a result, the total optical loss for such waveguides is lower than that for waveguides with a higher sidewall, which leads to an increase in the Q-factor of the microring resonator. However, a high aspect ratio worsens the mode localization, which leads to the need to significantly increase the bending radii of the waveguides.

The effect of scattering at the sidewall roughness can also be reduced by chemical etching of the oxide layer formed on the side surfaces of the silicon waveguides. Lee et al. [36] showed that high-temperature oxidation of integrated silicon waveguides in water and oxygen vapor followed by anisotropic etching resulted in a decrease in the sidewall roughness.

Accordingly, the optical loss in a single-mode silicon waveguide with a width of 500 nm was reduced to 0.8 dB cm^{-1}. Zhang et al. [68] studied microring resonators based on silicon with waveguide widths of 0.45, 1.6, and 2 μm. For these resonators, the measured Q-factors were 1.93×10^5, 2.73×10^6, and 3.95×10^6, respectively. Using these Q-factors, the optical losses were estimated at 1.6, 0.15, and 0.1 dB cm^{-1}. The sidewall and planar surface roughness values were 2.6 and 0.24 nm, respectively. As is known, an increase in the optical path length in a microring resonator leads to a decrease in the FSR, which for these resonators was 325 pm. Luo et al. [69] studied theoretically and experimentally a microresonator made on the basis of a wide (2 μm) shallow etched waveguide with a rib height of 130 nm and a lower layer height of 90 nm. The measured Q-factor of the microresonator was 1.01×10^6. The use of such a narrow-band filter made it possible to fabricate a temperature detector with a sensitivity of 0.019 °C.

For the development of band-pass optical filters used for dense wavelength division multiplexing (DWDM systems [70]), of interest is the problem of controlled tuning of the optical resonance width of a microring resonator. One of the methods for tuning the width of optical resonances is to change the coupling coefficient of the directional coupler of the ring resonator. However, when varying the coupling coefficient, not only does the resonance width change, but so does its height (depth). For example, Shoman et al. [71] developed a silicon microring resonator with an interferometrically tunable directional coupler. This design made it possible to change the optical resonance width in the range from 23.3 to 69.5 GHz by continuously changing the coupling coefficient from 0.114 to 0.453. In this case, the resonance height changed in the range of 2–30 dB. For independent control of the resonance width and depth, an 'add-drop' configuration of a ring resonator is used by synchronously adjusting the coupling coefficients of two directional couplers [72]. Chen et al. [72] demonstrated continuous tuning of the resonance width in the range of 0.1–0.7 nm (12.4–86.6 GHz) at a constant resonance height of 23 dB. Yao et al. [73] presented an interesting design of a silicon microtoroidal resonator. In this paper, the coupling coefficient of the directional couplers is changed using microelectromechanical systems (MEMSs), which leads to a continuous change in the optical resonance width in the range of 2.8–78.5 GHz while maintaining the resonance height of 21.8 dB. Yao et al. [73] experimentally showed that, with an increase in the resonance width, the insertion optical loss increases from 1.5 to 7.5 dB. It is possible to increase the tuning range of the width by producing complex integrated structures. Thus, Li et al. [74] demonstrated a silicon Mach–Zehnder interferometer, in the arms of which microring resonators with interferometrically tunable directional couplers are embedded. By synchronously changing coupling coefficients of directional couplers, the authors achieved a continuous change in the resonance width in the range of 0.46–3.09 nm (57.8–388.3 GHz) at a resonance height of 25 dB.

An alternative method for producing an integrated optical filter with a variable bandwidth based on a silicon microring resonator consists in combining two or more resonators with a constant-width resonance and changing the position of the

resonances relative to each other. This method allows one to significantly increase the form factor of the resonances — the ratio of the width at a height of 1 dB to the width at a height of 10 dB — and make the passband more rectangular. For example, Dai et al. [75] developed an optical filter containing four add-drop microring resonators, the spectral positions of the resonances of which are changed using four independent heaters. As a result, the resonance width was tuned in the range of 0.6–2.4 nm (75–300 GHz). The insertion optical loss was 1.23–6.3 dB, and the height of the optical resonances was obtained in the range of 16–20 dB. Ong et al. [76], by cascading two microring filters with tunable resonance positions, fabricated an optical filter with a tunable bandwidth in the range of 0.1–1 nm (12–125 GHz). In this case, the insertion loss was 3 dB.

4. Vernier filters with thermo-optical tuning

Tunable optical filters operating in the C + L band are being developed and fabricated and find application in optical spectrum analysis, wavelength division multiplexing, and sensor technology [77]. Key characteristics of such filters include the Q-factor, FSR, range, tuning speed, and efficiency. Microring resonators are often used as the main elements of tunable filters implemented in integrated designs. An effective method for tuning the resonant wavelength of microring resonators is the thermo-optic effect, which, as discussed above, consists of changing the refractive index of a substance with a change in temperature. The thermo-optic effect in silicon provides the greatest change in refractive index among existing materials [78]. Obvious advantages of this method, from the point of view of PIC fabrication, include minimal insertion optical loss, since the microheating element can be placed at a sufficient distance from the integrated waveguide.

For a microring resonator on a silicon-on-insulator substrate, variation in refractive indices of silicon and silicon dioxide changes the effective index of the ring waveguide and, consequently, changes the position of the resonant wavelength in the spectrum:

$$\Delta\lambda_{\text{res}} = \frac{\Delta n_{\text{eff}} L}{m}\,, \qquad m = 1, 2, 3\ldots\,, \tag{12}$$

where $\Delta n_{\text{eff}} = (\partial n_{\text{eff}}/\partial T)\Delta T$. Here, $\partial n_{\text{eff}}/\partial T$ is the effective thermo-optical coefficient of the waveguide mode. For waveguides on an SOI platform, the effective thermo-optical coefficient can be splitted into two terms containing the parameters of silicon and the dielectric [79]:

$$\frac{\partial n_{\text{eff}}}{\partial T} = \frac{\partial n_{\text{eff}}}{\partial n_{\text{Si}}}\frac{\partial n_{\text{Si}}}{\partial T} + \frac{\partial n_{\text{eff}}}{\partial n_{\text{SiO}_2}}\frac{\partial n_{\text{SiO}_2}}{\partial T}\,, \tag{13}$$

where $\partial n_{\text{Si}}/\partial T$ and $\partial n_{\text{SiO}_2}/\partial T$ are the thermo-optical coefficients of silicon and silicon dioxide. The thermo-optical coefficient of silicon dioxide is an order of magnitude smaller than that of silicon, and so its contribution is insignificant [78, 79].

The obtained thermo-optical shift of the resonance wavelength for silicon microring resonators was approximately 0.1 nm K^{-1} [24]. The silicon-on-insulator platform is the most promising for the fabrication of ring resonators with thermo-optical tuning and devices based on them due to the high thermo-optical coefficient of silicon. For comparison, the thermo-optical coefficient of silicon (1.86×10^{-4} K^{-1}) is almost 7.6 times higher than that of silicon nitride (2.45×10^{-5} K^{-1}) [78, 80]. As noted above, the SOI platform provides a high contrast of the refractive indices of silicon and silicon dioxide. This allows the fabrication of very compact microring resonators with small radii reaching values on the order of 1.5 μm, which corresponds to an FSR of 60 nm or higher [57]. However, thermo-optical tuning of the resonance wavelength of single microring resonators in such a wide range (about 60 nm) is associated with the need to heat the microring waveguide to high temperatures exceeding 500 °C, which is difficult to implement in an integrated design and requires a high power supply. For example, to shift the resonance wavelength in the optical spectrum by 10 nm, the power released on the microheater can reach 100 mW. For practical applications when developing a PIC with several ten or hundreds of tunable optical filters, the total power consumption can be very high.

Some applications require tuning an optical filter to a fairly large spectral range (for example, more than 60 nm). One of the optical techniques that allows markedly increasing an optical filter's FSR and, accordingly, its tuning range is the Vernier method [81]. It consists of two microring resonators with different radii and, as a result, different FSRs. The maximum transmission of the filter is observed if the resonance wavelengths of both resonators are matched. In the case of independent thermo-optical tuning of each resonator, it is possible to ensure continuous tuning of the resonance of the Vernier filter in the entire FSR. In this case, the radii of the microring resonators are selected so that the ratios of the circumferences are the ratio of integers [82]:

$$\frac{L_2}{L_1} = \frac{m_2}{m_1}\,. \tag{14}$$

Then, the resulting FSR of the Vernier filter will be determined as

$$\text{FSR}_{\text{Vernier}} = m_1 \text{FSR}_1 = m_2 \text{FSR}_2\,. \tag{15}$$

For the Vernier filter to be continuously tuned, it is necessary that both microring resonators be tuned in a range no less than the value of each FSR.

Figure 4 shows an optical microscope image of a typical structure of a Vernier filter fabricated on an SOI substrate [52]. Fiber-to-chip coupling is implemented using integrated diffraction gratings optimized for efficient TE- and TM-mode coupling in the case of silicon with thicknesses of 220 and 500 nm, respectively. The passive part is fabricated using electron beam lithography and plasma-chemical etching. Thermo-optical tuning of each microring resonator was performed using an independent metal heating element consisting of a titanium section located directly above the microring resonator and gold supply contacts. The heating elements are separated from the silicon passive part by a dielectric layer to minimize optical loss.

Vernier filters with different ratios of the microring resonator radii providing a system FSR from 45 to 90 nm have been fabricated and studied. Figure 5 shows characteristic transmission spectra of the optical filter, demonstrating thermo-optical tuning of the resonance wavelength of the Vernier filter in the range of 53 nm. For this structure, the FSRs of the microring resonators are 9 and 11 nm, while the FSR of the Vernier filter is about 53 nm. The experimentally measured tuning speed for the Vernier filters was higher than

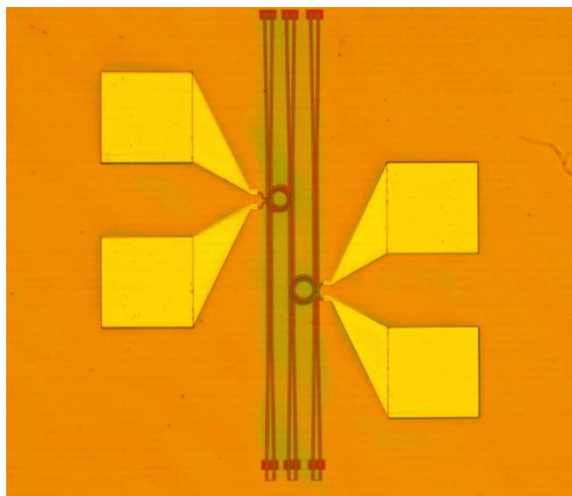

Figure 4. Optical image of integrated optical Vernier filter with two microheaters.

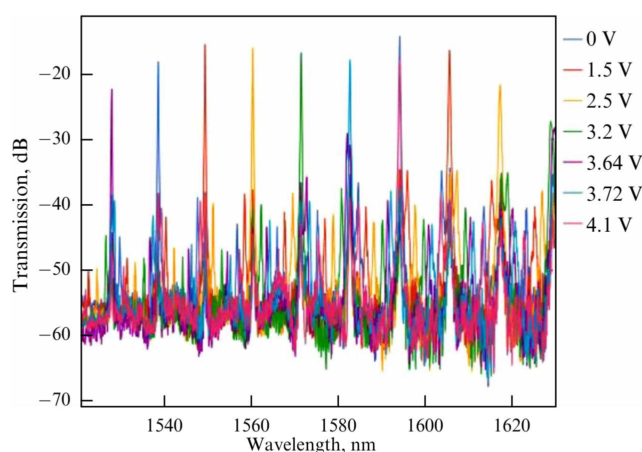

Figure 5. Optical transmission spectrum of integrated optical Vernier filter.

2 nm μs^{-1}. It is important that the value of the side peak suppression in the obtained spectra exceed 18 dB, and the spectral width of the optical resonance at half-maximum of the peak be less than 150 pm [52]. For comparison, Boeck et al. [51] studied a Vernier filter based on two microring race-track resonators fabricated on an SOI substrate with a 220-nm-thick working layer. The filter's FSR was 36 nm, the side peak suppression was more than 9 dB, and the width of the main resonance at half maximum was 740 pm. The optical loss in the structure presented in [52], minus the loss of the measuring equipment and the loss of scattering in the lensed fibers and diffraction gratings, was on average 3 dB for a set of ten structures. The configuration of the heating elements manufactured in these structures ensures tuning of the resonance wavelength of each microring resonator by at least 11 nm. In this case, the tuning efficiency was 130 pm mW^{-1}, which is more than 1.5 times higher than the efficiency demonstrated in [82, 105] (80.2 pm mW^{-1}).

5. Arrayed waveguide gratings

An arrayed waveguide grating (AWG) makes it possible to spectrally select a desired wavelength range. The main purpose of AWGs is the redistribution of input broadband radiation into spatially separated spectral channels. Such

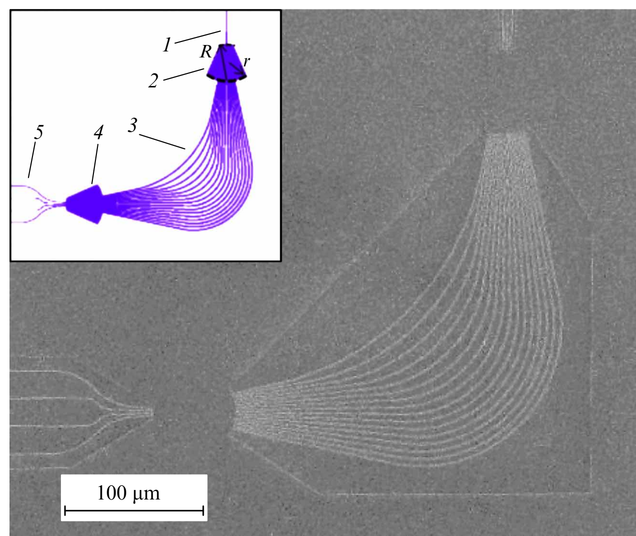

Figure 6. SEM image of incompletely etched arrayed waveguide grating. Shown in inset are *1*—input waveguide, *2*—splitter, *3*—intermediate waveguides, *4*—combiner, and *5*—output waveguides.

AWGs can be used as multiplexers and demultiplexers in integrated photonic circuits for data transmission, spectrum analyzers, and other devices [83–85].

The manufactured arrayed waveguide grating (Fig. 6) is an integral structure consisting of an input waveguide (*1*), a splitter (*2*), intermediate waveguides (*3*), a combiner (*4*), and output waveguides (*5*). The constituent elements of the ordered waveguide grating are calculated from analytical formulas, taking into account diffraction loss, propagation loss, scattering, and radiation loss at waveguide bends. The geometric size of the AWG elements are simulated depending on the desired parameters: the spectral width of the channels and the free spectral region of the AWG. The splitter (*1*) and combiner (*4*) are regions of free space propagation inside the silicon layer. These regions are formed by Rowland circles of radii R and r, with $R = 2r$. In the splitter region, the input radiation is diffracted into a multitude of intermediate waveguides. Varying the width of the waveguide at the input of the splitter changes the divergence of the input radiation.

The number of intermediate waveguides must correspond to the radiation diffraction region. To reduce the loss, intermediate waveguides in the junction region with the splitter and combiner are most often broadened. Electromagnetic radiation is distributed into intermediate waveguides with the same initial phase. The differences among the optical lengths of the intermediate waveguides set the phase difference of radiation propagating in parallel intermediate waveguides and is determined by the formula $m\lambda_0/n_{\text{eff}}$, where m is an integer, λ_0 is the center wavelength in a vacuum, and n_{eff} is the effective refractive index of the waveguide mode [86]. The intermediate waveguides of an arrayed waveguide grating can have a geometry with one or two roundings. If the intermediate waveguides have two roundings that are the same for all, the differences among the lengths of the waveguides are included in the length of the straight sections. In the case of one rounding, additional calculations are needed to correctly account for the difference in the lengths of the waveguides on segments of circles of different radii.

In the combiner region, multibeam interference occurs of radiation emerging from the intermediate waveguides with

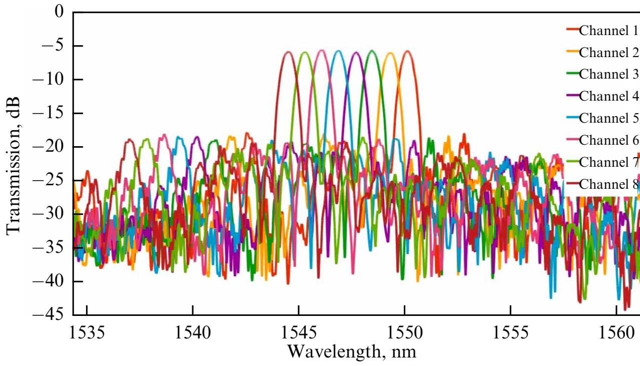

Figure 7. Optical transmission spectrum of an arrayed waveguide grating with a channel width of 100 GHz.

phases specified by the lengths of the corresponding waveguides. The receiving waveguides are located in the regions of interference maxima for a given wavelength of radiation at the combiner boundary. Crosstalk depends on the fraction of radiation that is incident into the adjacent output waveguides during interference and reflections in the combiner area. The distance between the output waveguides affects the crosstalk. The spectral distance between the centers of the output channels is specified at the design stage of the AWG and is determined by the phase difference in radiation in adjacent intermediate waveguides. The free spectral range of the arrayed waveguide grating should be greater than the spectral sum of the output channels.

Figure 6 shows an example of an integrated dense wavelength division multiplexing (DWDM) arrayed waveguide grating. The 1×8 arrayed waveguide gratings were calculated and manufactured with a spectral channel width and a distance between adjacent channels of 100 GHz. The crosstalk in the fabricated structure was 12.5 dB, and the total optical loss in the integrated structure was measured at the level of 5.5 dB. The level of optical loss in the structure can be reduced, for example, by decreasing the transverse size of the arrayed waveguide grating.

As noted above, due to the high optical contrast, arrayed waveguide gratings on an SOI platform are smaller than other integrated platforms. Table 2 compares integrated AWGs manufactured on various technological platforms for DWDM applications with a spectral channel width of 100 GHz.

As shown above, spectral multiplexing of channels on an integrated SOI platform can be implemented, for example, using a cascade of single or dual microring resonators. This scheme can provide a distance between adjacent channels of less than 100 GHz with a crosstalk of less than 60 dB [92]. A disadvantage of a cascade of microresonators as a demultiplexing is associated with the thermal stabilization of each microring resonator.

In DWDM optical communication lines, use can also be made of echelle gratings. These diffraction gratings can significantly improve the level of crosstalk, but have a larger footprint than an arrayed waveguide grating. The level of the crosstalk in echelle gratings is estimated to be 55–60 dB [93, 94], but the best integrated structures manufactured on the SOI platform demonstrate a crosstalk of −35 dB at a relatively large size of about 25 mm^2 [95].

Shallow etched arrayed waveguide grating, shown in Fig. 6, has a characteristic size of $\sim 350 \times 350$ μm^2. It is shown that the production of a splitter and combiner of an arrayed waveguide grating without sidewalls — limited only by intermediate and input (output) waveguides located along the circumference — leads to a decrease in the overall level of optical loss and the level of crosstalk in the structure, and the technology of incomplete etching on the SOI platform makes it possible to reduce the crosstalk and inserted loss between output waveguides to a level of −16 dB and −2.5 dB, respectively [96].

6. Interferometers and electro-optical modulators

Many optical systems that allow information to be transmitted and processed [97] or various signals to be modified [98] are of great scientific and practical interest, especially if the device is implemented as a compact photonic integrated circuit [99–101]. An optical modulator is used as the main component of such devices.

Existing electro-optical modulators manufactured on the indium phosphide platform are based on n–i–p–n heterostructures and demonstrate a wide bandwidth larger than 85 GHz, relatively moderate optical loss of about 6.1 dB, and extinction of greater than 33 dB [102]. Ozaki et al. [102] ascertain that a coherent transmitter based on such modulators is capable of transmitting information at a rate of 1 Tb s^{-1} per spectral channel, which is undoubtedly a high figure. To date, a bandwidth of higher than 100 GHz with an optical loss of less than 0.5 dB and extinction of about 30 dB in the active region has been demonstrated on a thin-film lithium niobate platform [103]. Good electro-optical characteristics of lithium niobate modulators and significant technological challenges that prevent the development of high-quality passive optical elements on this platform are driving researchers to search for hybrid solutions. In this approach, passive optics and low-speed thermo-optical tuning are implemented on the basis of silicon or silicon nitride platforms, while high optical signal processing rates are achieved in a lithium niobate layer integrated into these platforms. This solution made it possible to demonstrate modulation of optical radiation in a 37-GHz band on silicon nitride with an insertion optical loss

Table 2. Comparison of characteristics of AWGs having a spectral spacing of 100 GHz between channels and manufactured on different technological platforms.

Technological platform	Inserted loss, dB	Crosstalk, dB	AWG characteristic size, mm^2
Silicon on insulator (SOI) [87]	4.5	−20.5	1.26×0.9
Indium phosphide InP [88]	3.4	−14	4.3×0.6
Silicon nitride Si_3N_4 [89]	1.7	−21	2.2×0.7
Silicon dioxide SiO_2 [90]	2.0	−35	13×16
PMMA resist [91]	3.3	−11.6	15×9.2

of the modulator at a level of 1 dB and extinction of greater than 30 dB [104].

There are several types of integrated modulators on the SOI platform, based on the effects of electrorefraction (the real part of the refractive index changes) or electroabsorption (the imaginary part of the refractive index changes) [105]. Electrorefractive modulators include structures based on thermo-optical [85] and plasma dispersion [106] effects and plasmonic devices based on organic electrooptical compounds [107]. Some designs of such modulators have a fiber input interface in the form of a gold grating capable of exciting a plasmonic mode [108]. Among electroabsorption integrated modulators, hybrid structures based on silicon waveguides and transparent conducting oxides (TCOs) are quite popular; their properties can be either dielectric or metallic, depending on the concentration of free charge carriers. The operating principle of these modulators is based on the effect of changing the concentration of carriers at the dielectric–TCO layer boundary [20, 109, 110].

A controlled change in the refractive index of silicon due to temperature variation (thermo-optic effect) is used to control the optical response of spectrally selective silicon-based devices, for example, in Mach–Zehnder interferometers (MZI) or microring resonators. As noted above, the thermo-optic coefficient $\alpha = \partial n/\partial T$ — the dependence of the refractive index of the material n on temperature T — for silicon is 1.86×10^{-4} K^{-1} [64, 111]. This value is significantly higher than the thermo-optic coefficient of waveguide materials of other technological platforms. For example, the thermo-optic coefficient of silicon nitride is an order of magnitude smaller and is 2.45×10^{-5} K^{-1} [78, 80]. Heating of waveguide structures, for example, using a microheater, leads to a change in the refractive index and, consequently, this affects the value of the effective index and phase of the optical mode. Phase control using the thermo-optical effect in the MZI allows one to vary the intensity of the output optical radiation.

Figure 8a shows a diagram of an MZI with two heaters located above each arm of the interferometer. The results of an experimental study of optical transmission of the manufactured device are shown in Fig. 8b. The device is a modulator based on a Mach–Zehnder interferometer with thermo-optical control and is characterized by an extinction value of ~ 25 dB and a characteristic switching time of about 10 µs. The thermo-optical effect allows relatively slow optical modulation to be implemented, and such modulators can be used in areas where high data transfer rates are not required.

Plasmon modulators based on transparent conducting oxides are characterized by a small size, on the order of several microns, and a wide modulation band of higher than 40 GHz [109, 110]. A typical design of a modulator of this type includes layers of TCO, dielectric, and gold deposited on a waveguide in such a way as to form a flat capacitor [20, 109]. When voltage is applied to the capacitor, a thin layer appears with a concentration of free charge carriers in the TCO at the boundary with the dielectric such that conditions for the formation of a surface plasmon polariton are created. The electric field of the plasmon mode excited in the structure is largely concentrated inside the layers of the dielectric and TCO. The transformation of the waveguide mode into a plasmon mode, depending on the voltage on the capacitor and the parameters of the charged layer, provides amplitude modulation of the optical signal.

The condition for excitation of the plasmon mode is realized when the plane of radiation polarization is perpendicular to the modulator layers. Thus, modulation of the TE-polarized waveguide mode requires a capacitor geometry with plates adjacent to the vertical walls of the waveguide, which poses certain difficulties from a technological point of view. The TE-polarized waveguide mode can also excite the plasmon mode in the planar configuration of the capacitor, but this implies a special 'coupling interface' formed, for example, using edge plasmons [20].

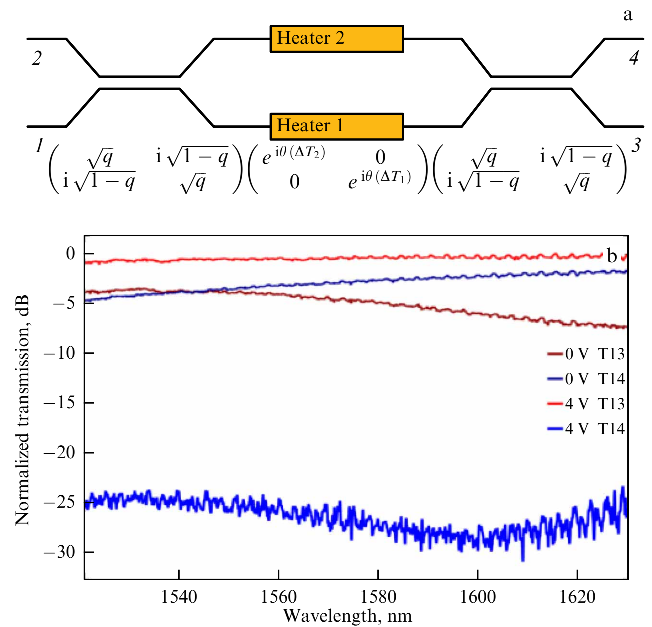

Figure 8. (a) Schematic of MZI with thermo-optical control and transmission matrices of its main elements, where q is the coupling coefficient of a directional coupler, and $\theta(T_1)$ and $\theta(T_2)$ are the phase shift of optical modes of heated waveguides. (b) Transmission spectra from port *1* to port *3* (T13) and from port *1* to port *4* (T14) at voltages of 0 and 4 V on heater 1.

Zemtsov et al. [109] designed, manufactured, and experimentally studied a plasmonic electroabsorption modulator based on a hybrid waveguide containing silicon and layers of dielectric (SiO_2) and indium tin oxide (ITO). The structure has a 'coupling interface' for the TE waveguide and surface plasmon modes. However, the hybrid waveguide configuration provides the ability to modulate the TM waveguide mode, which is a significant improvement over existing plasmonic modulators adapted only to a certain polarization of radiation. Figure 9 shows (a) a SEM image of the fabricated modulator obtained using a scanning electron microscope, (b) a schematic representation of the cross section of the modulation region, and results of measuring (c) the extinction coefficient and (d) the modulation bandwidth of the electro-optical modulator for the TE-polarized waveguide mode of optical radiation. The 15-µm-long modulator demonstrates an optical signal transmission of -4.6 ± 0.2 dB and an extinction of 1.8 ± 0.2 dB at wavelengths from 1520 to 1630 nm in a range of applied voltages from -3 V to $+2$ V. In the modulation region, the silicon waveguide is not limited by the sidewalls (Fig. 9a). This made it possible to apply voltage to the active region of the modulator using a wide planar contact made of indium tin oxide. The configuration of the active region of the modulator and the supply contacts made it possible to demonstrate a modulation band of higher than 40 GHz at a level of -2 dB on an 8-µm-long modulator [109].

Among modulators on the silicon platform, the highest-speed structures are those based on electro-optical organic

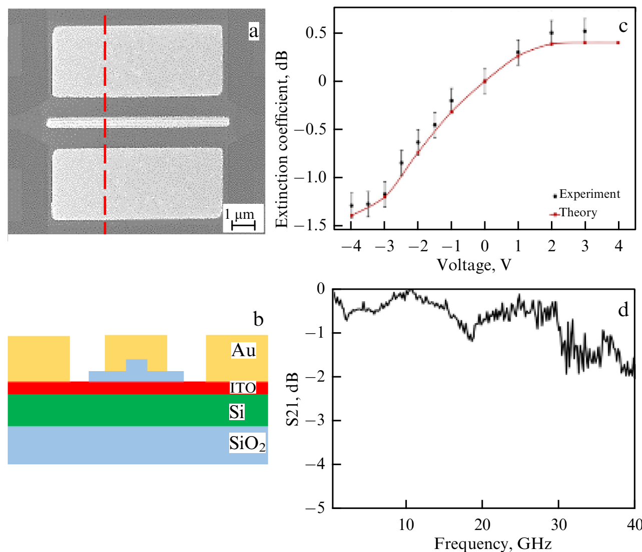

Figure 9. (a) SEM image of integrated electroabsorption plasmonic modulator; dashed line shows cross-sectional area for schematic image of modulation region cross section (b); (c) dependence of modulator extinction coefficient on applied voltage; and (d) normalized S21 response of analog optical path with an electroabsorption plasmonic modulator.

substances. The most popular and well-studied p–n and p–i–n structures are inferior to other modulators in terms of modulation bandwidth and size. Structures based on TCOs occupy the niche of the most compact high-speed integrated amplitude modulators with a full optical band (without resonant or asymmetric interference methods), possessing moderate extinction and optical loss. Below, Table 3 lists characteristics of modern high-frequency modulators manufactured on the SOI platform and operating in the optical C band (1528–1565 nm). In this review, we do not consider a fairly wide range of optical modulators based on graphene; hybrid cross-platform solutions, which are worthy of a separate review, are also outside the scope of this paper.

The main metric of the quality of the analog optical path is the free spectral range, which depends on the noise level and the transmission coefficient in the path, as well as on the magnitude of nonlinear distortions of the signal. The signal transfer coefficient of an analog optical path depends on the extinction coefficient of the modulator, the signal power loss in the path elements, and parameters of the amplifiers, photodetector, and laser used. In turn, the linearity of the path depends on the transfer function of the modulator, the linearity of the photodiode response, and the parameters of the amplifiers, provided that all other elements operate in linear regimes. A detailed description of issues related to the transfer coefficients, noise, and linearity in analog optical paths, as well as the relationship of these parameters with the characteristics of the modulator, can be found in book [115].

Properties of analog optical paths based on integrated Mach–Zehnder modulators (MZMs) have been studied relatively well. A path including a silicon dual-series MZM based on a p–n junction is capable of demonstrating a spurious-free dynamic range of more than 100 dB $Hz^{-2/3}$ at a frequency of 10 GHz for third-order intermodulation [116]. An analog optical path including a plasmonic MZM based on an electro-optical organic substance demonstrated a spurious-free dynamic range of 92.7 dB $Hz^{-2/3}$ [114]. The linearity and spurious-free dynamic range of paths with an integrated plasmonic modulator based on a transparent conducting oxide have not been fully investigated to date.

7. Optical coupling technologies

The high optical contrast of silicon compared to the surrounding waveguide dielectric materials (air or silicon dioxide) facilitates the fabrication of compact integrated optical devices. On the other hand, the small transverse size of the integrated elements leads to the problem of matching the sizes of optical modes between the silicon waveguide and the optical fiber. The area of the optical fiber core ($\sim$ 8 μm in diameter) is 450 times larger than the cross-sectional area of a single-mode integrated silicon waveguide (220×500 nm). This creates certain difficulties for the input and output of optical radiation in silicon-based photonic integrated circuits.

To solve this problem, use is usually made of diffraction gratings (vertical coupling) or spot-size converters (edge coupling) [117]. Diffraction gratings usually require a small angle of incidence of radiation to effectively implement input–output into/from the optical fiber. This leads to a technological problem in terms of coupling. The fiber must be positioned in the right place at the right angle, which means precise alignment in three spatial coordinates (usually with a tolerance of ± 1 μm) and three angles. In addition, the close-to-normal angle of incidence makes the final chip bulky and quite fragile. There is also an approach that ensures a perfectly vertical connection of the fiber to the chip, which somewhat simplifies the coupling process. In this method, use is made of a specially etched diffraction grating to ensure input–output at exactly 0° to the normal. Due to perfectly vertical input–output, angle alignment is practically eliminated, which minimizes the time needed for coupling and

Table 3. Comparison of characteristics of high-speed modulators on SOI platform.

Technology	Inserted loss, dB	Extinction coefficient, dB	Modulation bandwidth, GHz	Size, μm	Reference
p–n junction, ring resonator	1.5	23	60	8	[112]
p–n junction, symmetric MZM	8.4	20	47	2500	[113]
Plasmonic asymmetric MZM with organic electro-optical substance HD-BB-OH/YLD124	12.2	25	500	25	[114]
Plasmonic symmetric MZM with nonlinear electro-optical substance	30 (modulator and gratings)	15	70+ (limited by device)	20	[107]
Directional coupler, In_2O_3 TCO	4.5	1.7	40+ (limited by device)	7	[110]
Plasmonic interface, ITO TCO	4.6	1.8	40+ (limited by device)	15	[109]

reduces the overall complexity of the process. The input–output efficiency for a perfectly vertical coupling can reach 50–65% depending on the fiber used. Higher efficiency is achieved with lensed fiber, and lower, with conventional single-mode fiber. However, this approach does not solve the problem of the bulkiness and fragility of the final design. An example of a vertical method of radiation input–output in a PIC using an array of optical fibers fixed inside a glass block and grating couplers is given in [118].

Optical fiber-to-chip coupling using spot-size converters and lensed fibers demonstrates high efficiency of radiation input–output. McNab et al. [119] measured coupling loss at a level of −0.5 dB using a spot-size converter based on a polymer coating of a silicon waveguide with a so-called reverse taper. The advantage of end-to-end coupling also lies in the possibility of TE- and TM-polarized radiation input–output. However, as a rule, input efficiencies of different polarizations also differ. Note that this approach implies coupling to integral waveguides that are on the chip boundary. In addition, to implement end-to-end coupling, careful polishing of the sample edge and precise optical alignment of the optical fiber position relative to the silicon waveguide location in three coordinates and angles are needed, which significantly complicates the optical coupling technology.

A standard approach to horizontal coupling between optical fiber and a PIC is to use polished fibers. In this case, the fiber is polished at a certain angle, for example, 40° [120]. This ensures a beam deviation of 10° from the normal inside the fiber (and a resulting incidence angle of about 15° on the grating in the presence of an air gap), which is typical of standard grating couplers. Additional input–output coupling loss, arising from positioning errors, is less than 1 dB for a planar shift of less than 5 μm and also less than 1 dB for a vertical distance from the chip to a height of up to 13.5 μm. Therefore, this coupling method does not require high-precision positioning, as in the end-to-end coupling method. Advantages of this coupling method also include the ability to input–output optical radiation at any point on the sample surface. This method can be implemented with almost any PIC containing grating couplers, and a small number of functional elements reduces the complexity of manufacturing and assembly. UV-curable epoxy resin is used to fix fibers on the surface. It is also possible to use polished optical fiber arrays to provide input of several channels into the chip without any difficulties. However, this approach also has drawbacks. First, fiber polishing is not a standard procedure for CMOS technology in particular and silicon photonics in general. Second, the question remains open as to whether it is possible to accurately and reproducibly polish fibers at a certain required angle for production purposes. Although it has been shown that this can be achieved in small quantities, it is not known for certain whether this can be done in a cost-effective manner with large volumes of polishing.

One more widely used method for horizontal coupling between optical fiber and a PIC is the V-groove coupling technique using a tapered silicon waveguide — a mode converter [121]. Tapered waveguides offer a number of advantages over diffraction gratings. The largest potential advantage is the effective elimination of the polarization-dependent loss inherent in diffraction gratings. Another advantage is that tapered waveguides typically provide a much wider bandwidth, because they do not have the fundamental bandwidth limitations of diffraction gratings.

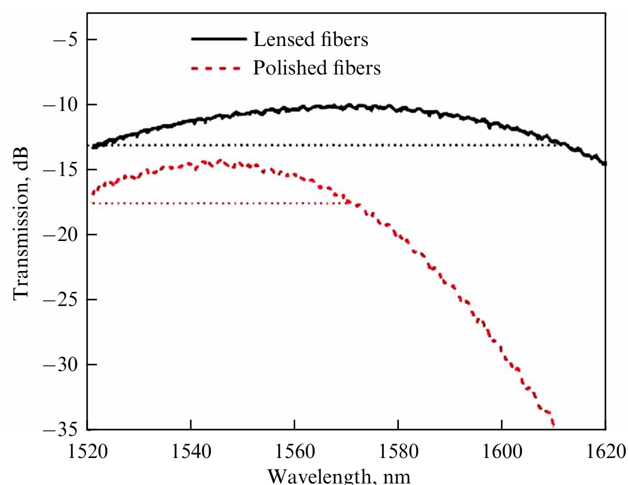

Figure 10. Transmission spectra of ‘optical probe–input diffraction grating–silicon waveguide–output diffraction grating–optical probe’ system for vertical (lensed fibers) and horizontal (polished fibers) coupling. Horizontal dotted lines show bandwidth at −3 dB level for each coupling method.

The V-groove in this method, which is formed by anisotropic etching of a silicon substrate, is used to fix the cleaved optical fiber. A tapered waveguide is used to gradually convert and match optical modes corresponding to the core of the optical fiber and the uniform-width silicon waveguide. The oxide waveguide layer underneath the tapered silicon waveguide works in such a way that the optical mode from the fiber smoothly passes into the oxide waveguide, because they have the same refractive index. Then, when optical mode in the oxide waveguide layer arrives on the inverted taper, it starts to gradually convert into the silicon waveguide mode with a higher effective refractive index until it is completely confined by the silicon waveguide. Theoretically, this process should occur adiabatically without energy loss. It is worth noting that the presence of a silicon substrate under the tapered silicon waveguide will act as a source of additional loss, since the mode radius in the optical fiber exceeds 4.6 μm and, therefore, this mode will leak into the substrate if the latter is not removed.

Of interest is a comparison of the efficiency of radiation input–output into/from a silicon waveguide using identical 7-μm-wide diffraction gratings for two cases: vertical coupling with lensed fibers oriented at a small angle to the normal (about 15°) and horizontal coupling with fibers polished at an angle of 40°. In both cases, a small (20–30 μm) air gap remained between the fibers and diffraction gratings. The measured transmission spectra are shown in Fig. 10. From the comparison of the optical spectra, it follows that the use of polished fibers leads to a decrease in the total transmission of the system by 4–5 dB, which corresponds to a decrease in the input–output coupling efficiency by 2–2.5 dB per grating. In addition, the bandwidth also decreases by about 50% compared to the case of vertical coupling using lensed fibers. Both of the above effects can be explained by more optimal matching of optical modes of fiber and the diffraction grating when using lensed optical probes that provide focusing of the radiation and a corresponding decrease in the mode field diameter (to 5–6 μm), as was shown in one of our recent papers [25]. Note that an increase in the width of the diffraction gratings from 7 to 15 μm allows the input–output

coupling efficiency to be increased by 2–3 dB for the case of horizontal coupling using polished fibers. This is explained by the divergence of the beam reflected from the polished surface of the fiber, which requires the use of a wider diffraction grating to ensure more efficient input–output radiation coupling into the silicon waveguide. However, an increase in the width of the input–output diffraction gratings does not affect the bandwidth. In this case, the bandwidth remains at a level typical for input–output of radiation using a cleaved fiber oriented at a small angle to the normal.

Advantages of optical radiation input–output through diffraction gratings include the possibility of integrating radiation sources and photodetectors directly onto a photonic integrated circuit. Heterogeneous and hybrid integration appear to be the most promising solutions for fabricating fully integrated photonic devices [13]. Heterogeneous integration involves bonding wafers of different materials directly or through an intermediate polymer layer, followed by the formation of structures using lithographic methods [122–125]. For example, a wafer of an A_3B_5 material with a gain medium for a laser is bonded to an SOI wafer. At this stage, precise alignment is not needed, since the resonator and other elements in the active layer are manufactured at later stages of high-resolution electron or optical lithography. Radiation input–output is implemented using evanescent pumping of an optical mode into a silicon waveguide or via diffraction gratings. This heterogeneous integration helps increase the density of elements on the wafer, but faces difficulties in ensuring the input–output coupling efficiency of radiation and a wider variation of device parameters compared to hybrid integration [13].

Hybrid integration involves combining two different chips containing, for example, a passive waveguide part formed in a silicon layer and active elements in the form of lasers and photodetectors manufactured on the A_3B_5 platform. This approach allows one to use most efficiently technological methods and solutions developed for various platforms and having their own individual characteristics, which often make it impossible, for example, to fully integrate the processes of structuring A_3B_5 materials into the technological line of silicon. Hybrid integration includes such methods as flip-chip bonding [126] or connecting two chips using an intermediate micro-optical system, for example, a mode converter based on a reverse taper or microlenses [127, 128].

Hybrid integration has proven itself well for the tasks of coupling lasers and photodetectors with a silicon platform. In the operating wavelength range of silicon photonics, photodetectors should be made of materials with a smaller band gap than that of silicon. In addition to A_3B_5 materials, germanium is suitable for the tasks of detecting radiation in the telecommunication wavelength range [129–131]. The advantage of germanium is its complete compatibility with silicon CMOS technology. In addition, germanium can be epitaxially grown on a silicon surface, which opens up prospects for its application not only for hybrid but also for monolithic heterogeneous integration into a silicon platform [132]. Comparative characteristics of avalanche germanium–silicon and A_3B_5 integrated photodiodes are presented in review [133]. Li et al. [134] presented a photodetector based on a p–i–n structure formed in a GeSn layer epitaxially grown on an SOI substrate using molecular beam epitaxy. The photodetector has a number of advantages, such as a low dark current, a high sensitivity of 14 mA W^{-1}, and a wide bandwidth of 30 GHz at the -3 dB level. Chowdhury et al. [135] demonstrated a low-voltage avalanche germanium–silicon photodiode with a high sensitivity of 26 A W^{-1} and a bandwidth of more than 30 GHz. High sensitivity in combination with low noise characteristics of such photodiodes are of interest for optical receivers [136, 137].

8. Conclusions

Silicon integrated photonics technologies make it possible to develop compact and highly efficient components of photonic integrated circuits. Using numerical calculations, a number of optical components have been designed and fabricated, including integrated optical waveguides, microring resonators, arrayed waveguide gratings, optical filters, and electro-optical modulators. Silicon photonics technologies have advanced from the fabrication of individual elements to fully functional photonic integrated circuits and devices based on them. A special advantage is the possibility of integrating silicon photonic integrated circuits with CMOS technologies and packaging technologies of modern microelectronics. At the same time, silicon photonics is still at the stage of rapid development. A number of such studies are promising for applications. They include hybrid and monolithic integration with other technology platforms, such as A_3B_5, Si_3N_4, SiGe, and lithium niobate, and the development of integrated optical amplifiers, optical isolators, broadband modulators, photodetectors, tunable lasers, and multilayer photonic integrated circuits.

This study was supported by the Russian Science Foundation (grant no. 23-91-06301).

References

1. Horikawa T et al. *IEEE J. Select. Topics Quantum Electron.* **24** 8200415 (2018) https://doi.org/10.1109/JSTQE.2018.2819893
2. Shen Y et al. *J. Lightwave Technol.* **37** 245 (2019)
3. Rumley S et al. *J. Lightwave Technol.* **33** 547 (2015)
4. Zhang X et al. *Nature* **603** 253 (2022)
5. Rogers C et al. *Nature* **590** 256 (2021)
6. Poulton C V et al. *IEEE J. Select. Topics Quantum Electron.* **28** 6100508 (2022) https://doi.org/10.1109/JSTQE.2022.3187707
7. Harris N C et al. *Nanophotonics* **5** 456 (2016)
8. Sun J et al. *IEEE J. Select. Topics Quantum Electron.* **20** 264 (2013)
9. Seok T J et al. *Optica* **6** 490 (2019)
10. Chang Lin et al. *Opt. Photon. News* **33** (1) 24 (2022)
11. Vlasov Yu A, McNab S J *Opt. Express* **12** 1622 (2004)
12. Horikawa T, Shimura D, Mogami T *MRS Commun.* **6** 9 (2016)
13. Pavesi L, Lockwood D J (Eds) *Silicon Photonics III. Systems and Applications* (Topics in Applied Physics, Vol. 122) (Berlin: Springer, 2016) https://doi.org/10.1007/978-3-642-10503-6
14. Bogaerts W, Chrostowski L *Laser Photon. Rev.* **12** 1700237 (2018)
15. Landau L D, Lifshitz E M *Electrodynamics of Continuous Media* (Oxford: Pergamon Press, 1984); Translated from Russian: *Elektrodinamika Sploshnykh Sred* (Moscow: Fizmatlit, 2005)
16. Novotny L, Hecht B *Principles of Nano-Optics* (Cambridge: Cambridge Univ. Press, 2012)
17. Inan U S, Marshall R A *Numerical Electromagnetics* (Cambridge: Cambridge Univ. Press, 2011)
18. Pshenichnyuk I A et al. *Phys. Rev. B* **109** 035401 (2024)
19. Pshenichnyuk I A, Kosolobov S S, Drachev V P *Phys. Rev. B* **103** 115404 (2021)
20. Pshenichnyuk I A et al. *Phys. Rev. B* **100** 195434 (2019)
21. Pshenichnyuk I A et al. *Quantum Electron.* **48** 1153 (2018); *Kvantovaya Elektron.* **48** 1153 (2018)
22. Bogaerts W et al. *J. Lightwave Technol.* **23** 401 (2005)
23. Li C, Liu D, Dai D *Nanophotonics* **8** 227 (2018)
24. Bogaerts W et al. *Laser Photon. Rev.* **6** 47 (2012)
25. Zemtsov D S et al. *Opt. Lett.* **47** 3339 (2022)
26. Dumon P et al. *IEEE Photon. Technol. Lett.* **16** 1328 (2004)
27. Bojko R et al. *J. Vac. Sci. Technol. B* **29** 06F309 (2011)

28. Chen Y et al. *J. Micro/Nanolithogr. MEMS MOEMS* **8** 043060 (2009)
29. Lee D H et al. *J. Micromech. Microeng.* **25** 015003 (2014)
30. Li B et al. *Optik* **172** 777 (2018)
31. Bellegarde C et al. *IEEE Photon. Technol. Lett.* **30** 591 (2018)
32. Sparacin D K et al. *J. Lightwave Technol.* **23** 2455 (2005)
33. Cardenas J et al. *Opt. Express* **17** 4752 (2009)
34. Gao F et al. *Appl. Phys. B* **81** 691 (2005)
35. Takahashi J et al. *J. Vac. Sci. Technol. B* **22** 2522 (2004)
36. Lee K K et al. *Opt. Lett.* **26** 1888 (2001)
37. Hirayama N et al., in *2012 Intern. Conf. on Solid State Devices and Materials, September 25–27, 2012, Kyoto, Japan, Extended Abstracts* (Tokyo: The Japan Society of Applied Physics, 2012) p. 530, https://doi.org/10.7567/SSDM.2012.A-2-2
38. Barwicz T, Haus H A *J. Lightwave Technol.* **23** 2719 (2005)
39. Qiu C et al. *J. Lightwave Technol.* **32** 2303 (2014)
40. Hong S et al. *Photon. Res.* **10** 1 (2022)
41. Dong P et al. *Opt. Express* **18** 14474 (2010)
42. Su Y et al. *Adv. Mater. Technol.* **5** 1901153 (2020)
43. Tran M A et al. *Appl. Sci.* **8** 1139 (2018)
44. Ławniczuk K et al. *Adv. Opt. Technol.* **4** (2) 157 (2015)
45. D'Agostino D et al. *Opt. Express* **23** 25143 (2015)
46. Wörhoff K et al. *Adv. Opt. Technol.* **4** (2) 189 (2015)
47. Blumenthal D J et al. *Proc. IEEE* **106** 2209 (2018)
48. Zhu D et al. *Adv. Opt. Photon.* **13** 242 (2021)
49. Himeno A, Kato K, Miya T *IEEE J. Select. Topics Quantum Electron.* **4** 913 (1998)
50. Barwicz T et al. *Proc. SPIE* **6872** 68720Z (2008)
51. Boeck R et al. *Opt. Express* **18** 25151 (2010)
52. Smirnov A S et al. *Foton-Ekspress* (6) 139 (2023) https://doi.org/10.24412/2308-6920-2023-6190-139-139
53. Sun Y, Fan X *Anal. Bioanal. Chem.* **399** 205 (2011)
54. Carlborg C F et al. *Lab Chip* **10** 281 (2010)
55. Washburn A L, Gunn L C, Bailey R C *Anal. Chem.* **81** 9499 (2009)
56. Tahersima M H et al. *Nanophotonics* **8** 1559 (2019)
57. Xu Q, Fattal D, Beausoleil R G *Opt. Express* **16** 4309 (2008)
58. Li A et al. *Laser Photon. Rev.* **10** 420 (2016)
59. Taziev K R, Kosolobov S S, Drachev V P *Foton-Ekspress* (6) 106 (2023) https://doi.org/10.24412/2308-6920-2023-6190-106-106
60. De Heyn P et al., in *2011 Optical Fiber Communication Conf. and Exposition and the National Fiber Optic Engineers Conf., OFC/NFOEC 2011, Los Angeles, California, USA, 6–10 March 2011* (Piscataway, NJ: IEEE, 2011) p. 1701
61. Ehrlichman Y et al., in *2016 IEEE Intern. Topical Meeting on Microwave Photonics, MWP 2016, Long Beach, California, USA, 31 October – 3 November 2016* (Piscataway, NJ: IEEE, 2016) p. 95
62. Guillén-Torres M A et al. *IEEE Photon. Conf.* 336 (2014) https://doi.org/10.1109/IPCon.2014.6995381
63. Burla M et al., in *2016 IEEE Intern. Topical Meeting on Microwave Photonics, MWP 2016, Long Beach, California, USA, 31 October – 3 November 2016* (Piscataway, NJ: IEEE, 2016) p. 259
64. Griffith A et al. *Opt. Express* **20** 21341 (2012)
65. Jiang W C, Zhang J, Lin Q *Opt. Express* **22** 1187 (2014)
66. Blumenthal D J et al. *Proc. IEEE* **106** 2209 (2018)
67. Bauters J F et al. *Opt. Express* **19** 3163 (2011)
68. Zhang L et al. *Laser Photon. Rev.* **16** 2100292 (2022)
69. Luo H et al. *Front. Optoelectron.* **16** 4 (2023)
70. Treshchikov V N, Listvin V N *DWDM-Sistemy* (*DWDM Systems*) (Moscow: Tekhnosfera, 2021)
71. Shoman H et al. *Opt. Express* **27** 26661 (2019)
72. Chen L, Sherwood-Droz N, Lipson M *Opt. Lett.* **32** 3361 (2007)
73. Yao J, Wu M C *Opt. Lett.* **34** 2557 (2009)
74. Li X et al. *J. Opt.* **49** 427 (2020)
75. Dai T et al. *Opt. Lett.* **41** 4807 (2016)
76. Ong J R, Kumar R, Mookherjea S *IEEE Photon. Technol. Lett.* **25** 1543 (2013)
77. Ren Y et al. *IEEE Photon. Technol. Lett.* **31** 1503 (2019)
78. Cocorullo G et al. *Appl. Phys. Lett.* **74** 3338 (1999)
79. Popovic A, Ph.D. Dissertation (Cambridge, MA: MIT, 2008)
80. Arbabi A, Goddard L L *Opt. Lett.* **38** 3878 (2013)
81. Boeck R et al. *Opt. Express* **18** 25151 (2010)
82. Bélanger-de Villers S, Hould D, Shi W, in *Optical Fiber Communication Conf. OFC, 2019* (OSA Technical Digest) (Washington, DC: Optica Publ. Group, 2019) paper W2A.4
83. Weng S et al. *Photonics* **8** 214 (2021)
84. Zhang Z, Wang Y, Tsang H K *ACS Photon.* **8** 1251 (2021)
85. Zemtsov D S et al. *Foton-Ekspress* (6) 110 (2023) https://doi.org/10.24412/2308-6920-2023-6190-110-111
86. Zemtsov D S et al. *Foton-Ekspress* 6 (174) 173 (2021) https://doi.org/10.24412/2308-6920-2021-6-173-174
87. Xie C et al. *Opt. Laser Technol.* **163** 109330 (2023)
88. Han Q, Ménard M, Shi W *IEEE Photon. Technol. Lett.* **32** 1411 (2020)
89. Shang K et al. *IEEE Photon. J.* **9** (5) 1 (2017)
90. Hibino Y *IEEE J. Select. Topics Quantum Electron.* **8** 1090 (2002)
91. Juhari N et al. *AIP Conf. Proc.* **2203** 020046 (2020)
92. Dong P *IEEE J. Select. Topics Quantum Electron.* **22** 6100609 (2016) https://doi.org/10.1109/JSTQE.2016.2575358
93. Lycett R J et al. *IEEE Photon. J.* **5** 2400123 (2013) https://doi.org/10.1109/JPHOT.2013.2251874
94. Wang Y, Calabretta N *Opt. Lett.* **47** 5268 (2022)
95. Wang Y et al. *J. Lightwave Technol.* **42** 1538 (2024)
96. Zemtsova A K et al. *Foton-Ekspress* (6) 96 (2023) https://doi.org/10.24412/2308-6920-2023-6190-96-97
97. Dadashev M S et al. *J. Commun. Technol. Electron.* **68** 185 (2023); *Radiotekh. Elektron.* **68** 188 (2023)
98. Ghelfi P et al. *Nature* **507** 341 (2014)
99. Mehta N et al., in *2020 IEEE Symp. on VLSI Technology, Honolulu, HI, USA, 16–19 June 2020* (Piscataway, NJ: IEEE, 2020) p. 56
100. Shan W et al. *Opt. Express* **29** 3375 (2021)
101. Esman D J et al. *J. Lightwave Technol.* **33** 2256 (2015)
102. Ozaki J et al. *J. Lightwave Technol.* **41** 3290 (2023)
103. Wang C et al. *Nature* **562** 101 (2018)
104. Ruan Z et al. *Laser Photon. Rev.* **17** 2200327 (2023)
105. Reed G T et al. *Nature Photon.* **4** 518 (2010)
106. Soref R A, Bennett B *IEEE J. Quantum Electron.* **23** 123 (1987)
107. Ayata M et al. *Science* **358** 630 (2017)
108. Zemtsov D S et al. *Komp'yut. Opt.* **47** 224 (2023)
109. Zemtsov D S et al. *J. Lightwave Technol.* **41** 6310 (2023)
110. Amin R et al. *Optica* **7** 333 (2020)
111. Cocorullo G, Rendina I *Electron. Lett.* **28** 83 (1992)
112. Zhang Y et al. *Photon. Res.* **10** 1127 (2022)
113. Alam M S et al. *J. Lightwave Technol.* **39** 4270 (2021)
114. Burla M et al. *APL Photon.* **4** 056106 (2019)
115. Cox C H (III) *Analog Optical Links: Theory and Practice* (New York: Cambridge Univ. Press, 2004)
116. Zhang Q et al. *Opt. Lett.* **44** 23 5655 (2019)
117. Chrostowski L, Hochberg M *Silicon Photonics Design: From Devices to Systems* (Cambridge: Cambridge Univ. Press, 2015)
118. Zimmermann L et al., in *5th IEEE Intern. Conf. on Group IV Photonics, 17–19 September 2008, Sorrento, Italy* (Piscataway, NJ: IEEE, 2008) p. 371, https://doi.org/10.1109/GROUP4.2008.4638203
119. McNab S J, Moll N, Vlasov Yu A *Opt. Express* **11** 2927 (2003)
120. Snyder B, O'Brien P, in *Optical Fiber Communication Conf.* (OSA Technical Digest) (Washington, DC: Optica Publ. Group, 2012) paper OM2E.5, https://doi.org/10.1364/OFC.2012.OM2E.5
121. Galan J V et al., in *6th IEEE Intern. Conf. Group IV Photonics* (Piscataway, NJ: IEEE, 2009) p. 148, https://doi.org/10.1109/GROUP4.2009.5338334
122. Margalit N et al. *Appl. Phys. Lett.* **118** 220501 (2021)
123. Liang D, Bowers J E *Light Adv. Manuf.* **2** (1) 59 (2021)
124. Heck M J R et al. *IEEE J. Select. Topics Quantum Electron.* **19** 6100117 (2013)
125. Porter C et al. *APL Photon.* **8** 080902 (2023)
126. Marinins A et al. *IEEE J. Select. Topics Quantum Electron.* **29** 8200311 (2023)
127. Mack M et al., US Patent 8168939 (2012)
128. Snyder B, Corbett B, O'Brien P *J. Lightwave Technol.* **31** 3934 (2013)
129. Dehlinger G et al. *IEEE Photon. Technol. Lett.* **16** 2547 (2004)
130. Ahn D et al. *Opt. Express* **15** 3916 (2007)
131. Vivien L et al. *Opt. Express* **15** 9843 (2007)
132. Wang J, Lee S *Sensors* **11** 696 (2011)
133. Yuan Y et al. *J. Semiconductors* **43** 2 021301 (2022)
134. Li X et al. *Photon. Res.* **9** 494 (2021)
135. Chowdhury A et al., in *2022 Optical Fiber Communications Conf. and Exhibition, OFC* (Technical Digest Series) (Washington, DC: Optica Publ. Group, 2022) paper W3D.1, https://doi.org/10.1364/OFC.2022.W3D.1
136. Kang Y et al. *Nature Photon.* **3** 59 (2009)
137. Benedikovic D et al. *IEEE J. Select. Topics Quantum Electron.* **28** 3802508 (2022)